# NaTi$_2$(PO$_4$)$_3$/N-doped hard carbon nanocomposites with sandwich structure for high performance Na-ion full batteries

Rong Sun,[a] Xudong Zhang,*[a] Kwan San Hui,*[c] Keliang Zhang,[a] Guogang Xu,[b] Changgang Li,[a] Jingyun Ma,[a] and Wen He*[a]

[a]     Dr. R. Sun, Prof. X. Zhang, K. Zhang, C. Li, Dr. J. Ma, Prof. W.  He Institute of Materials Science and Engineering, Qilu University of Technology (Shandong Academy of Sciences), Jinan 250353, China, E-mail: hewen1960@126.com

[b]     Dr. G. Xu  College of Material Science and Engineering, Shandong University of Science and Technology, Qingdao 266590, China, E-mail: xgg_79@163.com

[c]     Dr. KS. Hui  Energy and Environment Laboratory, School of Engineering, University of East Anglia (UEA), Norwich, NR4 7TJ, United Kingdom. E-mail: k.hui@uea.ac.uk

Corresponding author E-mail address:  hewen1960@126.com

Supporting information for this article is given via a link at the end of the document.((Please delete this text if not appropriate))

**Abstract:** The well-matched technology of cathode and anode in Na-ion full batteries is highly challenging yet critically important in practical applications. Here, the high-performance Na-ion full batteries are developed by using NaTi$_2$(PO$_4$)$_3$/N-doped mesoporous hard carbon hybrid anode and porous Na$_3$V$_2$(PO$_4$)$_3$ cathode. The different anodes are designed for well-matched Na-ion full batteries. The unique sandwich and mesoporous structural features endow the hybrid anode with a high reversible capacity (240 mAh g$^{-1}$ at 1 C), high rate performance (109.7 mAh g$^{-1}$ at 100 C), utrahigh energy/power densities (76.56 W kg$^{-1}$/5104 W kg$^{-1}$) and a long cycle-life (capacity retention 92.1% after 1000 cycles at 100C) in a half cell. In a full battery, this hybrid anode can also deliver a higher capacitive contribution (79.5–87.7%) and high energy/power densities (104 Wh kg$^{-1}$/5256 W kg$^{-1}$). This design provides a promising pathway for developing high performance and low-cost Na-ion full batteries.

## Introduction

Pursuing higher energy density with no sacrifice of power density drives people to develop high-performance energy storage devices (HEDs) such as supercapacitors,[1] HEDs have attracted enormous attention due to its potential applications in future electric vehicles, smart electric grids, and even miniaturized electronic/optoelectronic devices, etc.[2] However, the availability of lithium leads to a quickly rising price of Li resources. So the development of high-performance HEDs is a great challenge for modern electrochemistry. Recently, low-cost Na-ion full batteries (SIFBs) with high energy/power densities, high rate performance and long cycling stability have attracted more and more interest and attention.[3] In view of numerous applications of Na-ion full batteries, there has been a great demand for high-performance hybrid electrodes with both high energy density and power density.[4] Among various HEDs, sodium-ion full batteries (SIFBs) with pseudocapacitive behaviour are currently considered to be an excellent candidate owing to their price, safety, long cycle life and environmental friendliness.[5]

In design and fabrication of low-cost SIFBs, the well-matched technology of cathode and anode is highly challenging yet critically important in practical applications.[6] Because the larger ionic radius of Na leads to a much more sluggish Na-diffusion kinetics, this makes the cathode difficult to match with some traditional anode materials of LIBs, so it is highly imperative to develop superior anode materials with unique structure.[7] Among various anode materials, the Na-superionic conductor (NASICON) structured compounds with the stable and open framework are attracting more and more attention owing to their large interstitial channels and high ionic mobility.[8] Among these compounds, NaTi$_2$(PO$_4$)$_3$ (NTP) has been proposed as a promising anode material due to its low cost, high abundance, high electrical conductivity and remarkable thermal stability for SIFBs . NTP has a "zero strain" frame structure that does not undergo volume expansion during the deintercalation reaction, which ensures its excellent rate performance, high energy density and long-term cycle life.[9] However, the inherent low electron conductivity of the phosphate backbone limits its application in high power sodium-ion batteries. In order to improve electron/ion transport kinetics of the NTP, several approaches have been attempted, such as the addition of various carbon materials (e.g., graphene, porous carbon, carbon nanotube, and so on),[10] nanocrystallization and porous structure of NTP.[11] Mai et al. synthesized carbon-coated hierarchical NaTi$_2$(PO$_4$)$_3$ mesoporous microflowers with superior sodium storage performance via a facile and controllable solvothermal method.[12] Besides, two-dimensional (2D) layered

NTP has excellent structural, electrochemical, and mechanical properties and can offer some advantages for Na storage, such as inhibiting the stacking of layered materials through the interaction with the carbon component, shortening the diffusion length of Na ions and facilitating the insertion/extraction of Na ions.[13] Despite all the efforts, NTP with both high energy and power densities as well as long cycling life has rarely been realized.

Chitosan, a soluble polysaccharide compound obtained by deacetylation of chitin has aroused considerable interests in synthesis of energy storage materials because of its unique properties and multiple functional groups.[14] Herein, we develop high energy/power density SIFBs by using $NaTi_2(PO_4)_3$ (NTP)/N-doped mesoporous hard carbon (N-MHC) hybrid anode and porous $Na_3V_2(PO_4)_3$ (PNVP) cathode. The novelty of this work is the unique sandwich structure of NTP/N-MHC nanocomposites prepared by using a chitosan-assisted sol-gel and subsequent calcination method, which greatly improves its rate performance and cycle stability. The challenge of this design is to retain efficient Na ion diffusion in NTP/N-MHC anode and PNVP cathode simultaneously. The well-matched technology issue of NTP/N-MHC anode with cathode is a crucial issue that the SIFBs can achieve both ultrahigh energy and power densities as well as long cycling life. Several merits of this design are as follows: (1) N-MHC (about 11.8 wt.%) provides high interface areas for the insertion/extraction of Na ions; (2) mesoporous structure makes the Na ions and electrolyte easily penetrate; (3) unique sandwich framework structure could be used as a stable scaffold for more Na-ion storage sites, fast electron transmission and $Na^+$ migration, which is the most significant factor for ultrahigh rate performance and excellent long cycling life; (4) N doping (2.02 wt.%) in MHC can ameliorate the electrochemical performance by adjusting the surface functional groups, enhancing electric conductivity, in favor of the charge transfer and electrode–electrolyte interactions;[15] (5) the multifunction chitosan is based on abundant renewable resource, which makes this synthesis technology simple and cost effective; (6) the all phosphate NTP anode and NVP cathode can exhibit zero-strain characteristics during charge and discharge cycles due to the inverse volume change, offering a safer and cycle stable Na-ion technology for SIFBs .[16] Owing to these merits, the SIFBs exhibit the ultrahigh energy and power densities, which are among the best thus far reported for SIFBs assembled with NTP anode (Table S1 in the Supporting Information lists some recently reported SIFBs assembled with NTP anode).

**Results and Discussion**

Chitosan-controlled the formation of sandwich structure and enhanced electrochemical performances of the NTP/N-MHC hybrid electrode were first demonstrated. The XRD patterns (Figure 1a) of different samples present their crystallographic phase and crystallinity. All the diffraction peaks in each sample are accurately indexed to the NASICON structured NTP with a hexagonal crystal system and R-3c space group (PDF #84-2009). All the sample have sharp and intense diffraction peaks, showing the well-crystallized characteristics. Furthermore, by comparison, it can be found that the 116 diffraction peak intensity of NTP/N-MHC-3 and NTP/C samples is significantly lower than that of NTP. The results calculated by using Jade 6 XRD pattern-processing software also show that NTP/N-MHC-3 has smaller crystallite size (43.5 nm) and higher crystallinity (90.81%) than NTP/C and NTP (Table S2). The crystallite size (43.5 nm) of NTP/N-MHC-3 is significantly lower than that (51.3 nm) of NTP. These indicate that and the crystal face growth of 116 was restrained in the synthesis. The element contents of the different samples were determined by using Vario EL IIICHN elemental analyzer (Table S3). The results show that NTP/N-MHC-3 has the carbon content of 11.8 wt% and the nitrogen content of 2.02 wt%.

In order to further analyze the composition and structure of carbon-wrapped layers，Raman spectra of different samples are shown in Figure 1b. Obviously, the spectra of both NTP/N-MHC-3 and NTP/C show two characteristic bands of carbon at about 1350 $cm^{-1}$ (D-band, disorder-initiated phonon mode) and 1600 $cm^{-1}$ (G-band, graphite band). Furthermore, the two broad peaks of each sample can be disassembled into four peaks by utilizing Gaussian numerical simulation (see the Supporting Information, Figure S2).[7] The sp3-type carbon (amorphous carbon and the defects) is correlated to two peaks around 1200 $cm^{-1}$ (1) and 1540 $cm^{-1}$ (3), while sp2-type carbon (graphitized carbon) is related to the other peaks around 1350 $cm^{-1}$ (2) and 1600 $cm^{-1}$ (4).[17] According to the peak area, the peak intensity ratios of the D-band and the G-band (ID/IG) of NTP/N-MHC-3 and NTP/C are 3.34 (Figure S2a) and 1.15 (Figure S2b), respectively. The ID/IG of chitosan after pyrolysis at 800 °C for 8 h is 3.03 (Figure S2c), which means that both chitosan after pyrolysis and residual carbon in NTP/N-MHC-3 are hard carbon (HC). The results show that the fraction of hard carbon (HC) in the residual carbon of NTP/N-MHC-3 is significantly higher than that of NTP/C, which contributes to improving the electronic conductivity and electrochemical performance of the hybrid electrode.[18] The HC layer in NTP/N-MHC-3 mainly originates from the carbonization of chitosan in the annealing process.
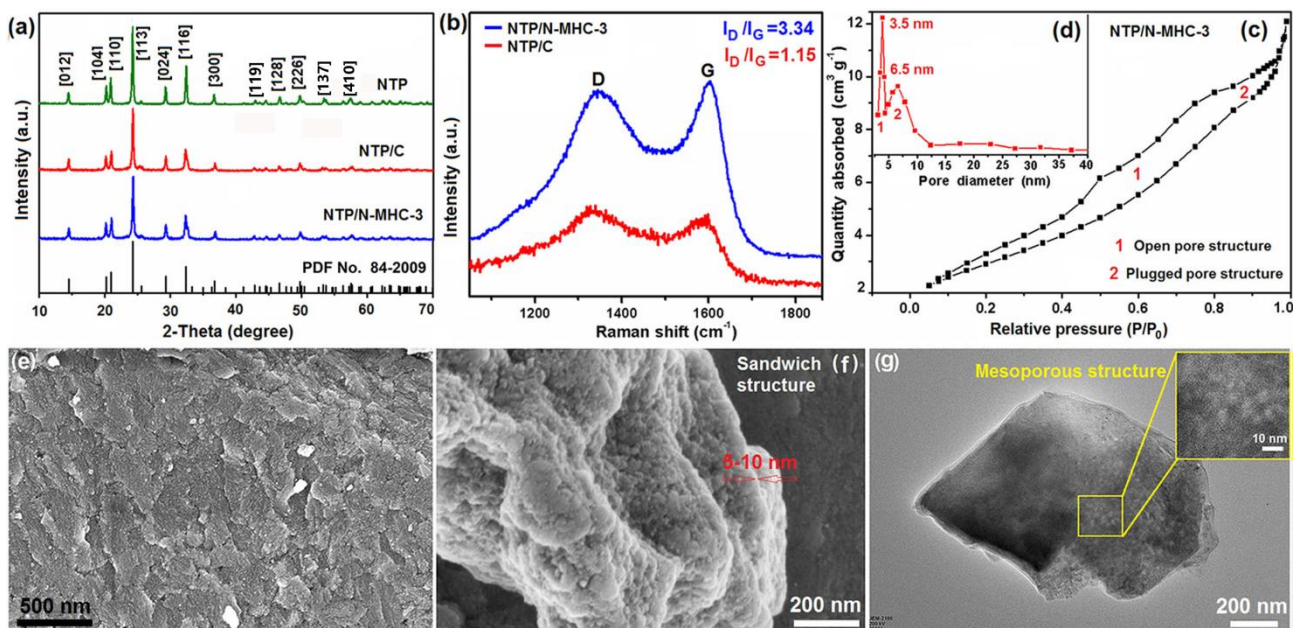
**Figure 1.** (a) XRD patterns of different samples. (b) Raman spectra of different samples. $N_2$ adsorption−desorption isotherm (c) and the pore-size distribution as the inset (d) of NTP/N-MHC-3. (e-f) SEM images of NTP/N-MHC-3. (g) TEM image of NTP/N-MHC-3.

So chitosan can be used as a hard carbon source in the synthesis of NTP/N-MHC.

To examine the mesoporous structure in NTP/N-MHC-3 sample, we perform nitrogen isothermal adsorption technique. According to the International Union of Pure and Applied chemistry regulation.[19] The NTP/N-MHC-3 sample shows a typical type IV hysteresis loop pattern that indicates mesoporous characteristics (Figure 1c). Its hysteresis loop consists of an open pore structure (region 1) and a plugged pore structure (region 2).[20] The Barrett–Joyner–Halenda pore-size-distribution curve of NTP/N-MHC-3 sample also displays a bimodal pore size distribution centered at 3.5 and 6.5 nm, respectively (Figure 1d). Due to the presence of mesopores, NTP/N-MHC-3 can significantly increase the permeability of the electrolyte, which makes Na ions in electrolyte easily react with NTP nanoparticles.

The detailed morphology and fine microstructure of NTP/N-MHC-3 are characterized by FESEM and HRTEM. The SEM images show that the NTP/N-MHC-3 has the laminar stack structure with the thickness of about 5–10 nm (Figure 1ef). The enlarged SEM image (Figure 1f) indicates the existence of many mesopores with the size of 2–10 nm on the laminar particles, which is consistent with the results of Figure 1cd. TEM image (Figure 1g) shows a particle with a multilayer structure and mesopores. Figure 2a is an HRTEM image recorded at a positive Scherzer defocus, which shows the disordered structure and vermicular texture on certain orientation in a HC ultrathin sheet. The inset in Figure 2a clearly displays C and N atomic columns. It is found that the N atomic columns show brighter spots because they have a higher atomic density than that of C

atom.[17] Figure 2b also manifests the NTP crystal nucleus formed on the surface of N-MHC (inset). Figure 2c clearly shows the lattice fringes of different crystal planes, corresponding to the (024) (A), (116) (B) and (110) (C) of different NTP nanoparticles (about 5–15 nm), respectively. The NTP nanoparticles are attached to the hard carbon layer, which promotes the diffusion of free electrons and sodium ions in the electrochemical process. The confined growth of NTP nanoparticles in a monolayer N-MHC sheet is also clearly observed from the HRTEM images (Figure S3ab). The SEM images in Figures 3a-c show that the chitosan after pyrolysis also has lamellar structure, which indicates that the chitosan template plays an important role in the sandwich structure formation of NTP/N-MHC-3.

According to the above characterization results, the synthesis mechanism of NTP/N-MHC is summarized in Figure 3d-i. Chitosan is used as a HC source, N source and a nucleating agent during the synthesis. The structure of chitosan has an ordered carbon compound backbone, which can be used as a structural template. It also owns many active groups, such as amino groups (-NH$_2$) and hydroxyl groups (-OH) (Figure 3d), which can adsorb TiO$_6$ and PO$_4$ ions and generate the cross-linking and sol-gel reactions (Figure 3e). So chitosan can effectively induce the nucleation of NTP sol particles, which also promotes the two-dimensional cross-linking reaction and self-assembly of chitosan. During pyrolytic degradation, the carbon compound backbone of chitosan is decomposed to form N-MHC with sandwich structure, while N-MHC can effectively restrict the growth of the NTP nanoparticles. Figure 3f shows a structure model of the NTP/N-MHC hybrid electrode, exhibiting the high-

efficiency electron/Na ion transport pathway for fast sodium insertion and abundant Na storage sites. So the NTP/N-MHC hybrid electrode exhibits excellent electrochemical performances (Figure 5). Figure 3g shows the adsorption assembly process of metal ion groups in the 2D cross-linked structure of chitosan during the synthesis reaction. The heterogeneous nucleation and confined growth of NTP nanoparticles in N-MHC are schematically illustrated in Figure 3hi, respectively.
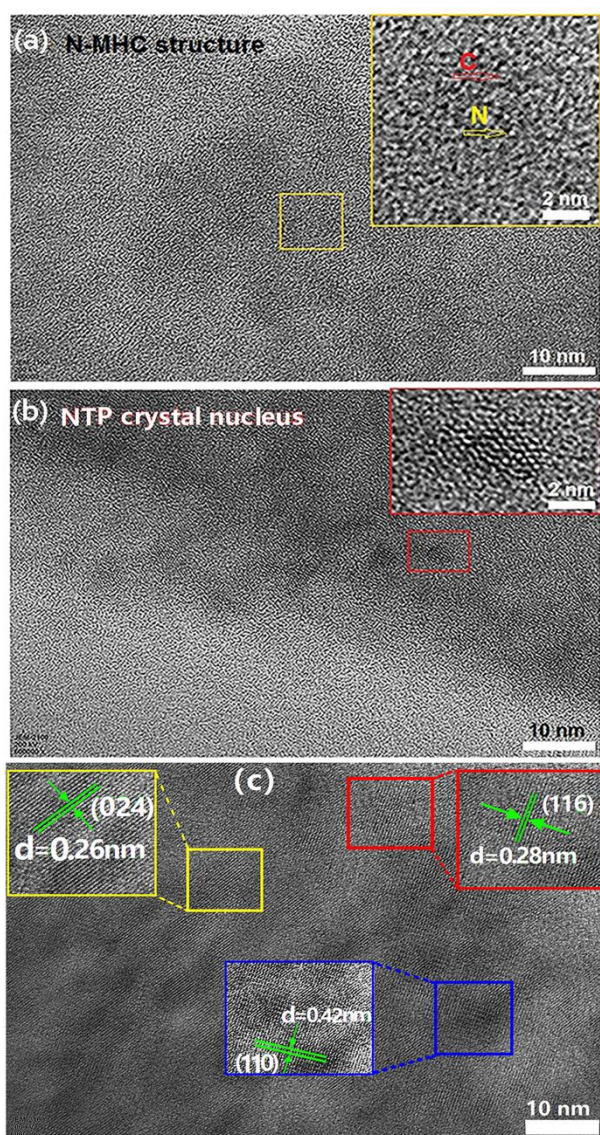


**Figure 2.** (a-c) HRTEM images of NTP/N-MHC-3.

The surface compositions and element distribution of NTP/N-MHC-3 sample are characterized by X-ray photoelectron spectroscopy (XPS), scanning-transmission electron microscopy (STEM) and X-ray energy dispersive spectrometry (EDS). Figure 4a shows a typical XPS survey spectrum of NTP/N-MHC-3 sample, indicating the presence of Ti, P, Na, O, C and N elements. However, the signal strength of Ti, P, Na elements is very weak because the NTP particles in NTP/N-MHC-3 were completely embedded in the interlayer of N-MHC. Figures 4b and Figure 4c show the deconvolution results of XPS Ti 2p and P 2p lines by using two curve fitting methods with nearly 100% Gaussian function, respectively. The two diffraction peaks at around 459.2 eV and 465.1 eV (Figures 4b) are assigned to Ti $2p^{3/2}$ and Ti $2p^{1/2}$ without evidence of impurities, respectively, which well consistent with the $Ti^{4+}$ in an octahedral environment of $NaTi_2(PO_4)_3$.[19] The two diffraction peaks at around 132.3 and 13.4 eV in the high resolution XPS spectrum of P2p are assigned to –P-O and –P=O groups, respectively, indicating that the P atoms are in an tetrahedral environment with +5 valance (Figures 4c). Figure 4d shows a high resolution XPS spectrum of Na 1s, implying that the Na atoms are with +1 valance. These XPS results further validate the XRD results in Figure 1a. The high-resolution XPS spectra of C1s, O 1s and N 1s for NTP/N-MHC-3 are shown Figure S4 a, b and c, respectively. The two diffraction peaks at around 283.8, 531 and 298.2 eV are assigned to C-C, O-H and N1 groups, respectively, indicating that there are atoms of C, H and N in NTP/N-MHC-3. These results are consistent with the results of Vario EL IIICHN elemental analyzer (Table S3). The EDS spectrum of NTP/N-MHC-3 sample in Figure 4e shows the peaks of titanium, phosphorus, sodium, oxygen, carbon and nitrogen, which further validate the XPS results (Figure 4a). The peaks of copper are assigned to the copper network supported the sample. Figure 4f shows a nanoparticle in NTP/N-MHC-3 sample and the elemental distributions of Ti, P, Na, O, C and N in this nanoparticle are shown in Figure 4g-l, respectively. It can be observed that the all elements are distributed homogeneously in this nanoparticle. Carbon is mainly distributed on the surface of this particle, and plays the role of adhesive and conductive agent. It can be observed that the all elements are distributed More importantly，N element is also distributed on the surface of this particle, forming N-doped carbon coating. These results show that the NTP nanoparticles were uniformly dispersed in the N-MHC, which is beneficial to improve the electrochemical performances of NTP/N-MHC-3.

First, optimization studies are carried out for the synthesis of NTP/N-MHC hybrid electrode by using the galvanostatic charge-discharge test. Figure S5 and Figure S6 show XRD patterns of different samples synthesized under different preparation conditions, and the all samples show characteristic diffraction peaks of NTP. The intensity of diffraction peaks all increases with the increasing of calcinations temperature and holding time, and the crystallite size of NTP also increases (Table S2). However, the NTP/N-MHC-3 sample synthesized with the chitosan content of 0.2 g at 800 °C for 8 h has smaller crystallite

4

size and higher crystallinity of NTP. Figure S7 shows the electrochemical performances of Na ion half-cells assembled with the different electrodes synthesized under the different preparation conditions and Na metal as the counter electrode in the voltage range of 0–3.0 V. The results indicate that the NTP/N-MHC-3 electrode synthesized with the chitosan content of 200 mg at 800 °C for 8 h has the best rate performance.
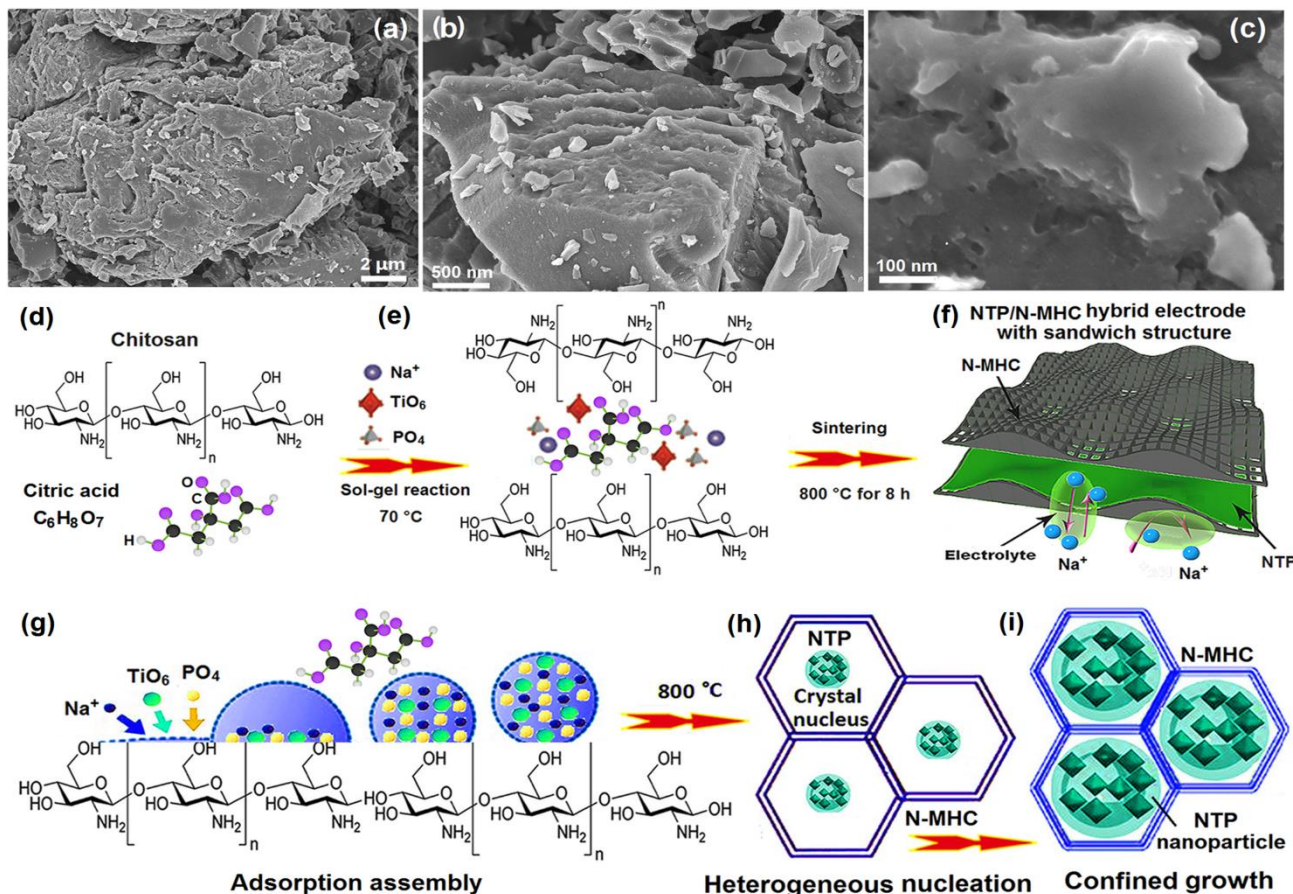
However, the rate performances of pure chitosan anode after pyrolysis at 800 °C for 8 h (Figure S8) is very poor and barely has capacity at the higher rates, which shows that it cannot be used as an anode alone. The electrochemical properties of the different electrodes were also evaluated in the Na ion half-cells and the voltage range of 1.5-3.0 V.



**Figure 3.** (a-c) SEM images of chitosan after pyrolysis at 800 °C for 8 h. (d) A schematic presentation of the multifunctional chitosan. (e) A schematic diagram of self-assembly of chitosan with some kinds of ions. (f) Structure model of NTP/N-MHC hybrid electrode. (g) Schematic diagram of the adsorption assembly process of metal ion groups in the 2D cross-linked structure of chitosan during the synthesis reaction. (h-i) Schematic diagrams of heterogeneous nucleation process (h) and confined growth process (i) of NTP nanoparticles in N-MHC.

Figure 5a shows the initial discharge-charge curves of different electrodes at 1 C. The first discharge capacity of NTP, NTP/C and NTP/N-MHC-3 was 19.3, 102.6 and 122.8 mAh g$^{-1}$, respectively. The corresponding Coulombic efficiency is 87.2%, 89.5% and 95.2%, respectively. Compared with NTP and NTP/C, the NTP/N-MHC-3 hybrid electrode not only exhibits the highest discharge capacity and the highest Coulombic efficiency, but also delivers a longer coupled flat plateaus at around 2.1 V, corresponding to the redox reaction of Ti$^{4+}$/Ti$^{3+}$.[9] Figure. S9a shows the cyclic voltammograms (CV) of different electrodes at a scanning rate of 0.2 mV s$^{-1}$ within the potential window of 1.5-3.0 V (vs Na/Na$^+$). All the electrodes show a pair of well-defined redox peaks at around 2.1 V, which characterize the oxidation

and reduction reactions of Ti$^{4+}$↔Ti$^{3+}$ through a two-phase reaction mechanism as represented by the Equation (1): [21]

$$NaTi_2(PO_4)_3 + 2Na^+ + 2e^- \rightarrow Na_3Ti_2(PO_4)_3 \qquad (1)$$

The Nyquist plots of different electrodes in the uncirculated state are shown in Figure S9b. They consist of a semicircle in the high-middle frequency range and a straight line in the low frequency region. The semicircle represents charge transfer resistance ($R_{ct}$) between the electrolyte and electrode. Compared with NTP and NTP/C, the NTP/N-MHC-3 not only shows a pair of sharp strong redox peaks (Figure S9a) with a larger peak potential difference, but also has the smallest $R_{ct}$ value (92 Ω) (Figure S9b). These indicate that the NTP/N-MHC-3 electrode has lower electrochemical polarization and higher
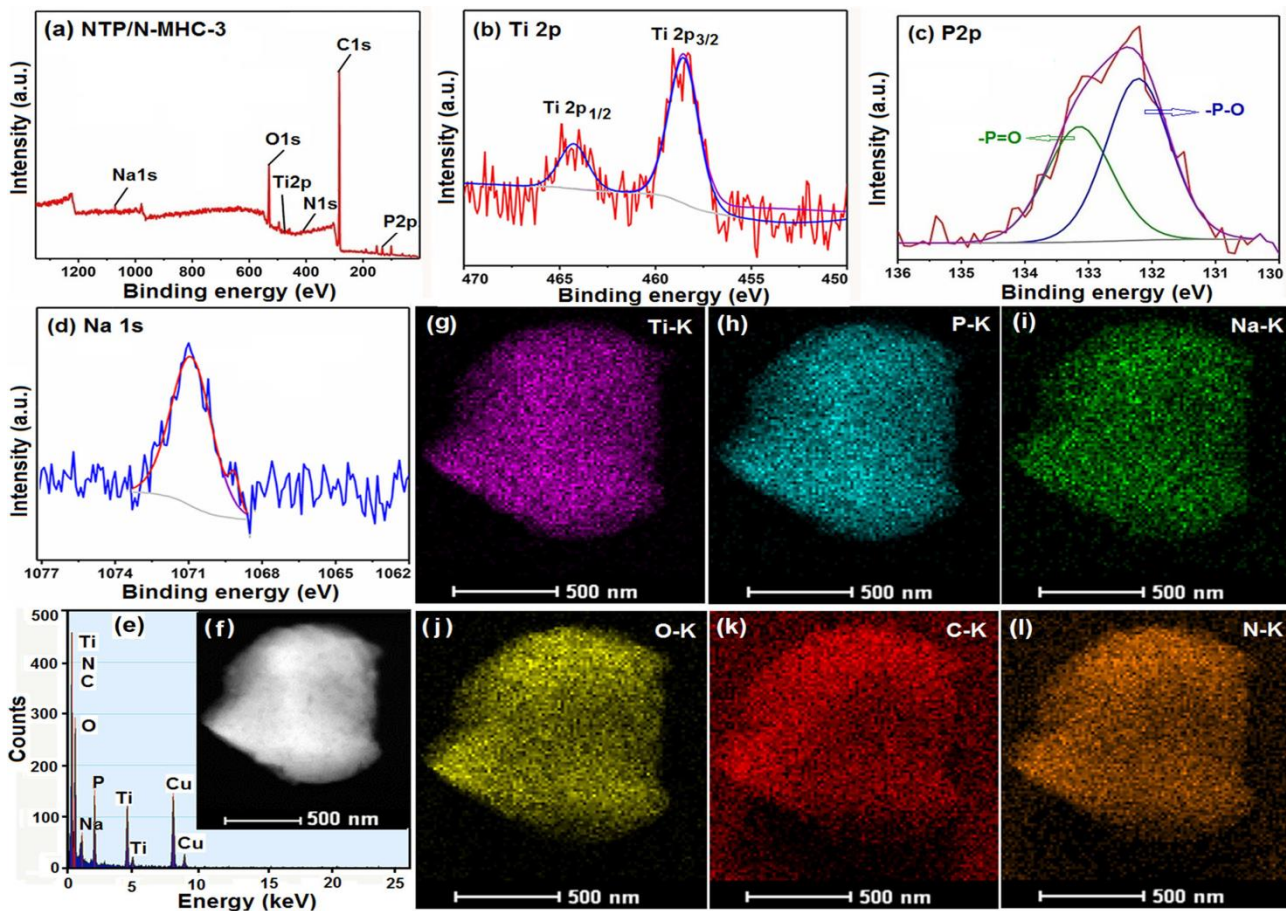
**Figure 4.** (a) Survey XPS spectrum of NTP/N-MHC-3 sample, (b-d) high resolution XPS spectra of elements in NTP/N-MHC-3 sample: Ti 2p (b), P 2p (c) and Na 1s (d). (e) EDS spectrum of NTP/N-MHC-3 sample. (f) STEM image of a nanoparticle in NTP/N-MHC-3 sample and (g–l) the elemental mapping images of this nanoparticle: titanium (g), phosphorus (h), sodium (i), oxygen (j), carbon (k), nitrogen (l).

reversibility due to the high conductivity of N-MHC framework, which effectively improves the electrochemical performance. The diffusion coefficient (D) of Na ions can be calculated from the plots in the low frequency region using the following equations: [22]

$$D = \frac{R^2 T^2}{2A^2 n^4 F^4 C^2 \sigma^2} \quad (2)$$

$$Z_{real} = R_e + R_{ct} + \sigma \omega^{1/2} \quad (3)$$

Where $R$ is the gas constant ($R$=8.314 J mol$^{-1}$ K$^{-1}$), $T$ is the temperature ($T$=298.15 K), $A$ is electrode area ($A$ =1.13 cm$^2$), $n$ is the number of electrons per molecule during oxidization ($A$ =1), $F$ is Faraday's constant $F$ =96486 C mol$^{-1}$). $\sigma$ is the Warburg factor which is obtained from the inset in Figure S9b. Based on the equation 3, the value of σ for NTP/C and NTP/N-MHC-3 is 382.53 and 38.07, respectively. Based on the equation 2, the value of $D$ for NTP/C and NTP/N-MHC-3 is 3.32×10$^{-14}$, 8.14×10$^{-13}$ cm$^2$ s$^{-1}$, respectively (Table S4). The calculation results show that NTP/N-MHC-3 has the higher diffusion coefficient of Na ion, indicating that the electrochemical kinetics of NTP/N-MHC-3 is much faster than that of NTP/C. The rate performances of

different electrodes are shown in Figure 5b. Table S5 shows magnification, current density and theoretical capacity of the half battery in the voltage range of 0.01–3.0 V. The results show that the NTP/N-MHC-3 has higher rate performance than other samples. When the current rate is increased from 1C (200 mA) to 100 C (20 A), the discharging capacity of NTP/N-MHC-3 is reduced from 123 mAh g$^{-1}$ to 113 mAh g$^{-1}$. Especially when the high current rates increase continuously from 20 C to 100 C, the attenuation rate of its charging capacity is very low. The energy and power density of the different electrodes are calculated from the discharge curves at various current densities (Figure 5c). [23] The energy density and power density of NTP/N-MHC-3 hybrid electrode are superior to other electrodes. The NTP/N-MHC-3 hybrid electrode has a high energy density of 253 Wh kg$^{-1}$ at a power density of 203 W kg$^{-1}$ (1 C), which also remains 196 W h kg$^{-1}$ even at ultrahigh power density of 17816 W kg$^{-1}$ (Table S6).

To gain further insight into the electrochemical kinetics of Na$^+$ insertion, the CV curves of NTP/N-MHC-3 hybrid electrode at different scan rates in a voltage range of 1.5–3.0 V are shown in Figure S9c. As increasing the scanning rate from 0.5 to 4 mV s$^{-1}$,
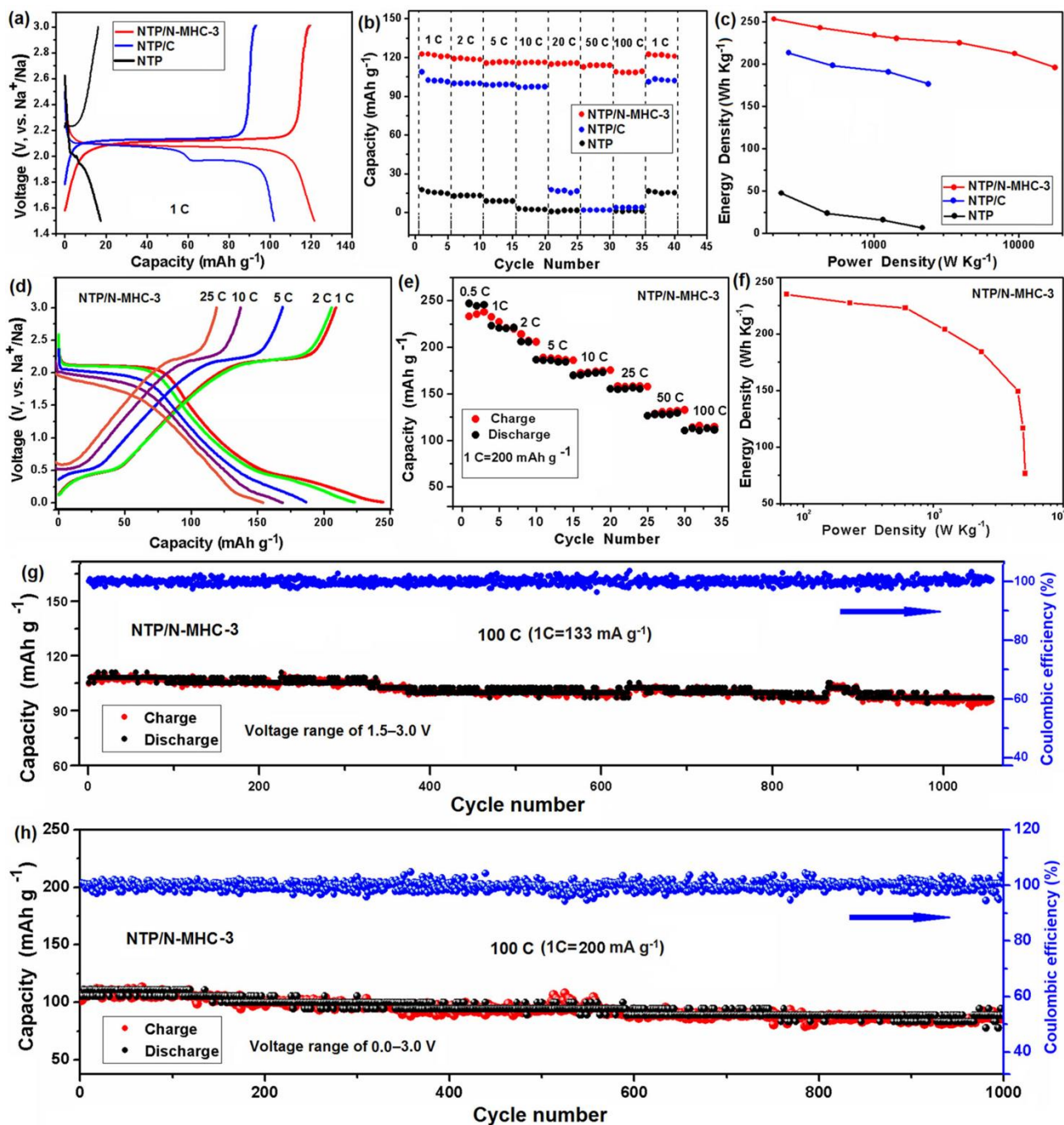
**Figure 5.** (a) The initial charge-discharge curves of different electrodes in the voltage range of 1.5–3.0 V at 1 C. (b) The rate performances of different electrodes in the voltage range of 1.5–3.0 V, showing the charging capacity. (c) Ragone plots (energy density vs. power density) of different electrodes in the voltage range of 1.5–3.0 V. (d) The charge-discharge curves of NTP/N-MHC-3 electrode at the different rates in the relatively wide voltage range of 0.01–3.0 V. (e) The rate performances of NTP/N-MHC-3 electrode in the relatively wide voltage range of 0.01–3.0 V. (f) Ragone plots (energy density vs. power density) of NTP/N-MHC-3 electrode in the relatively wide voltage range of 0.01–3.0 V. (g) The cycling performance of NTP/N-MHC-3 electrode at 100 C (1C=133 mA g-1) in the voltage range of 1.5–3.0 V. (h) The cycling performance of NTP/N-MHC-3 electrode at 100 C (1C=200 mA g-1) in the relatively wide voltage range of 0.01–3.0 V.

the oxidation and the reduction peaks move in the positive and negative directions, respectively, which means that the polarization increases as the scan rate increases. Moreover, it also remains a pair of well-defined redox peaks even at an ultrahigh scanning rate of 4 mV s⁻¹, showing good reproducibility and better chemical reversibility.[9] Figure S9d shows the linear relationship between the peak currents and the square root of the scan rate for the oxidation (A) and reduction (B) peaks. At the same time, the sodium ion diffusion coefficient (D) can be calculated on the basis of the Randles Sevick equation (4): [21]

$$I_P = 2.69 \times 10^5 An^{3/2}C_{Na}D^{1/2}v^{1/2} \tag{4}$$

Where $A$ is the effective area of the electrode (cm$^2$), $n$ is the number of electron transfer of the electrode reaction, $v$ is the scan rate (v s$^{-1}$), $C_{Na}$ is the concentration of the reactant (mol cm$^{-3}$), and $Ip$ is the peak current (A). Thus, the $D$ values calculated by using A and B peaks are 8.205×10$^{-10}$ and 6.553×10$^{-9}$ cm$^2$ s$^{-1}$, respectively, which shows that the reduction reaction is faster than the oxidation reaction. It is important that the NTP/N-MHC-3 hybrid electrode still realizes a ultra-long cycling ability at the ultra-high C-rates. As shown in Figure S9, the first-cycle charge capacity of 109.3mAh g$^{-1}$ for NTP/N-MHC-3 in the voltage of 1.5-3.0 V at 20 C. After 1000 cycles, the charging capacity was 104.9 mAh g$^{-1}$, and the capacity retention rate was 95.4%. Even at an ultrahigh rate of 100 C, it still shows the first-cycle charge capacity of 105.1 mAh g$^{-1}$, and also remains the charging capacity of 96.9 mAh g$^{-1}$ and the capacity retention rate of 92.1% after 1000 cycles (Figure 5g). The results show that the NTP/N-MHC-3 hybrid electrode has extremely high rate performance and cycle stability. The electrochemical performances of the NTP/N-MHC-3 hybrid electrode were also investigated using half cells vs. Na/Na$^+$ in a relatively wide voltage range of 0.01–3.0 V, as shown in Figure 5d-f. The results show that the discharging capacity of NTP/N-MHC-3 can reach 240 mAh g$^{-1}$ at 1 C (200 mA g$^{-1}$) (Figure 5de). Figure S10a shows the CV curves of NTP/N-MHC-3 electrode at different scan rates in a relatively wide voltage range of 0.01–3.0 V. By fitting the linear relationship between the peak currents ($I_P$) and the square root of the scan rate ($v^{1/2}$) for A and B peaks (Figure S10b), the calculated $D_{Na}$ values are 6.97×10$^{-9}$ and 8.995×10$^{-9}$ cm$^2$ s$^{-1}$, respectively. The two obvious redox peaks are observed at about 0.6/0.24 and 2.3/1.7 V, corresponding to the oxidation and reduction of Ti$^{3+}$↔Ti$^{2+}$ in 0.01–1.0 V and Ti$^{4+}$↔Ti$^{3+}$ in 1.5–3.0 V (Equation (1)), respectively. The reaction mechanism that Ti$^{3+}$ ions can be further reduced to Ti$^{2+}$ in 0.01-1.0 V is represented by Equation (5):

$$Na_3Ti_2(PO_4)_3 + Na^+ + e^+ \rightarrow Na_4Ti_2(PO_4)_3 \quad (5)$$

Interestingly, the third reduction peak can be detected near 0 V, which is ascribed to Na$^+$ storage in the interlayer of NTP/N-MHC.[11] NTP/N-MHC-3 hybrid electrode not only delivers excellent rate capability (Figure 5e) and high energy density/power densities (Figure 5f and Table S7), but also better cycle stability at an ultrahigh rate of 100 C (Figure 5h). The energy density of NTP/N-MHC-3 hybrid electrode in the voltage range of 1.5–3.0 V reaches up to 253 Wh kg$^{-1}$ at the power density of 204 W kg$^{-1}$. Highly encouragingly, its energy density can still maintain 196 Wh kg$^{-1}$ when offering a tremendous power density of 17816 W kg$^{-1}$ (Table S6). Its energy density

retention reaches up to 77.5%. To our surprise, such power capability even exceeds capacitors. The results show that the attainment of both high power and high energy densities in the NTP/N-MHC-3 hybrid electrode can be achieved, which is attributed to its unique sandwich and mesoporous structures.

To develop low-cost and intrinsically safe SIFBs with fast rechargeable, long cycling stability and high energy density, we study the matched technology of the electrode configuration in SIFBs and construct a high-performance SIFBs using an NTP/N-MHC-3 anode and PNVP cathode with a mass ratio of 1:1.2 (NTP/N-MHC//PNVP). Figure. 6a shows the CV curves for the NTP/N-MHC-3 anode and PNVP cathode, which display a pair of redox peaks near 2.1 V and 3.4 V, corresponding to the redox of Ti$^{3+}$/Ti$^{4+}$ and V$^{3+}$/V$^{4+}$, respectively.[16] The occurrence of double reduction peaks in the CV curve of NVP cathode is due to the ion rearrangement of Na2 in the discharge process.[8] Figure 6b is the CV curve of NTP/N-MHC//PNVP full battery in the voltage range of 0.4−2.0 V. vs Na/Na$^+$, showing a pair of well-defined redox peaks at 1.35/1.20 V. Figure 6b also shows that there is a pair of very small peaks at high voltage region, which may be due to the valence state changes of titanium ions. These show that the anode is perfectly matched with the cathode in the NTP/N-MHC//PNVP full battery. Figure 6d presents the long-term cycling performance of the NTP/N-MHC//PNVP full battery in the voltage of 0.4-2.0 V at 20 C (1C=117 mAh g$^{-1}$). After 1000 cycles, the charging capacity was 54.9 mAh g$^{-1}$, and the capacity retention rate is 81.6% with the Coulombic efficiency of 99%, exhibiting highly reversible Na storage performance. Furthermore, Figure 6d also shows a gradual increase in the charge/discharge capacity of the NTP/N-MHC//PNVP full battery before pre-sodium with the increase of cycle numbers, i.e., a reversible capacity of 69 mAh g-1 at 20 C and nearly 47.5% capacity increase after 150 cycles. This phenomenon is attributed to continuous activation process of NTP/N-MHC-3 anode and PNVP cathode because the unique sandwich structure structure and porous structure could provide abundant defects and electrochemical active sites. The electrolyte with the increase of cycle numbers was constantly immersed into the defects and pore structure, leading to the increase of contact area between electrolyte and electrode materials and storage sites for Na ion, and hence, there is a gradual increase in the capacity.[21] To understand the Na$^+$ diffusion properties in the charge and discharge cycle of NTP/N-MHC//PNVP full battery, the EIS measurements were carried out before and after 1000 charge/discharge cycles at 20 C (Figure 6c). The Nyquist plots show that the charge transfer resistance ($R_{ct}$) before and after 1000 cycles are 98 and 95 Ω, respectively. Based on the

equations of 2 and 3, the calculated D Navalue before and after 1000 cycles only reduced from $1.05\times10^{-13}$ to $1.22\times10^{-13}$ cm$^2$ s$^{-1}$ (inset in Figure 6c and Table S4). Thus, the change of $D_{Na}$ and $R_{ct}$ values further indicates that the full cell has good electrochemical cycle stability.
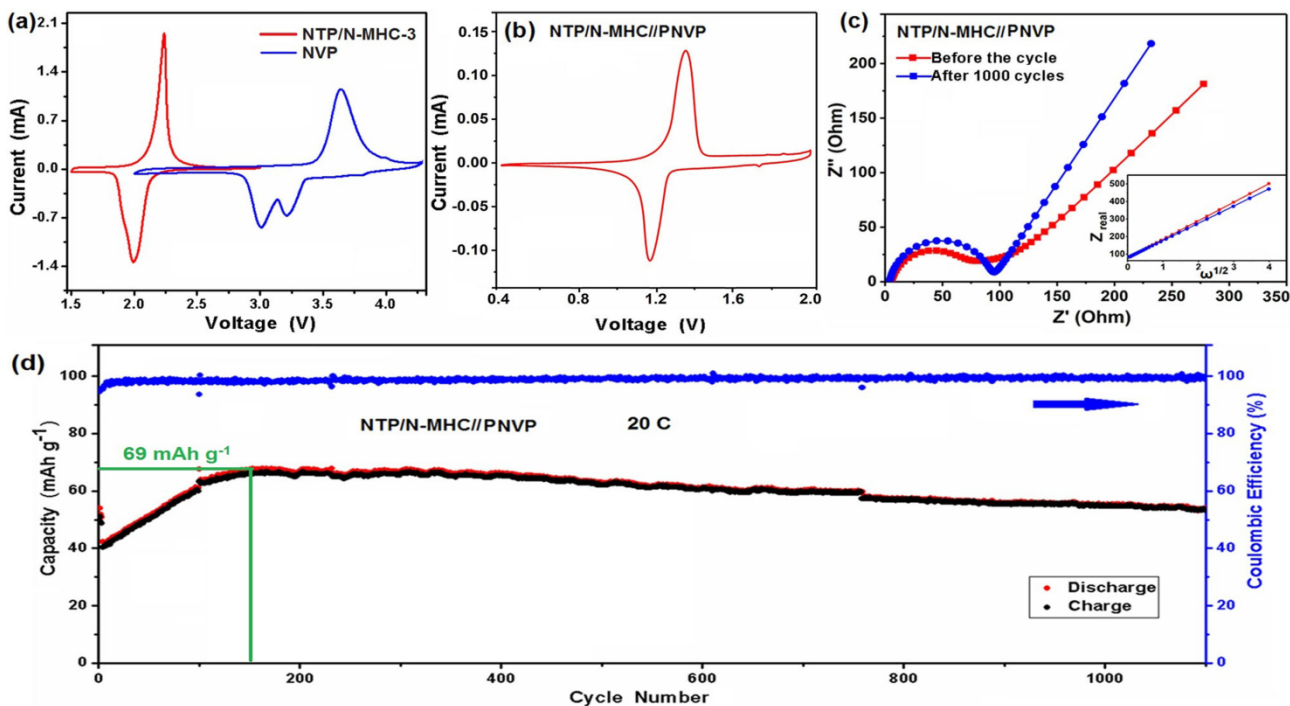


**Figure 6.** (a) The CV curve comparison of NTP/N-MHC-3 anode and NVP cathode at the scan rate of 0.5 mV s-1. (b) The CV curve of NTP/N-MHC//PNVP full battery at the scan rate of 0.1 mV s-1. (c) The Nyquist plots of NTP/N-MHC//PNVP full battery before and after 1000 charge/discharge cycles, the inset of (c) shows the plots of impedance as a function of the inverse square root of angular frequency in the Warburg region. (d) The cyclic performance chart of NTP/N-MHC//PNVP full battery at 20 C (1C=117mAh g-1).

To expatiate the energy storage mechanism, we compared the electrochemical performances of NTP/N-MHC//PNVP full battery before and after pre-sodium. Figure 7a shows that the charge and discharge curve of NTP/N-MHC//PNVP full battery before pre-sodium at 0.1 C only has a coupled flat plateau with the charge/discharge of 100/91.3 mAh g$^{-1}$ at around 1.25 V, but that of NTP/N-MHC//PNVP full battery after pre-sodium has two charging plateaus at around 2.75 and 3.25 V, respectively. The charging capacities of NTP/N-MHC//PNVP full battery before and after pre-sodium at 0.1 C is 100 and 80 mAh g$^{-1}$ respectively. Figure 7a shows that the charge and discharge curve of NTP/N-MHC//PNVP full battery before pre-sodium at 0.1 C also has some plateaued at lower voltage region of 0.5−1.0 V, which may be caused by pseudocapacitive behavior of N-MHC and are well corresponding to the results in Figure 8. The CV curves of NTP/N-MHC//PNVP full battery before and after pre-sodium at the scan rate of 0.1 mV s$^{-1}$ exhibit that the battery before pre-sodium shows a pair of coupled redox peaks around 1.17/1.35 V (Figure 7b), agreeing well with the discharge-charge curves (Figure 7a), but the battery after pre-sodium shows two pairs redox peaks at around 2.80/2.90 and 3.25/3.38 V, respectively. The results of Nyquist plots (Figure 7c) show that the

$R_{ct}$ (86 Ω) of NTP/N-MHC//PNVP full battery after pre-sodium are much smaller than that of the full battery before pre-sodium (258Ω). Based on the equations of 2 and 3, the value of $D$ for the NTP/N-MHC//PNVP full batteries before and after pre-sodium is $3.32\times10^{-14}$, $8.14\times10^{-13}$ cm$^2$ s$^{-1}$, respectively (Figure 7d and Table S4). The calculation results show that the NTP/N-MHC//PNVP full battery after pre-sodium has the higher diffusion coefficient of Na ion, indicating that the electrochemical kinetics of the full battery after pre-sodium is much faster than that of the full batteries before pre-sodium.

Figure 7e shows the charge and discharge curves of NTP/N-MHC//PNVP full battery before pre-sodium at different scan rates in the voltage of 0.4−2.0 V. The battery polarization reasonably increased with increasing the current rate from 0.1 C to 5 C, and the charge/discharge capacities reduced to 50/58 mAh g$^{-1}$ (5 C rate). Although the pre-sodium for NTP/N-MHC//PNVP full battery leads to the lower charging/discharging capacity and the poorer rate performance (Figure 7f), its energy and power densities were obviously improved because the number and voltage of redox plateaus increased (Figure 7g). Tables S8 and S9 show the detailed comparison data of energy and power density of NTP/N-MHC//PNVP full battery before and
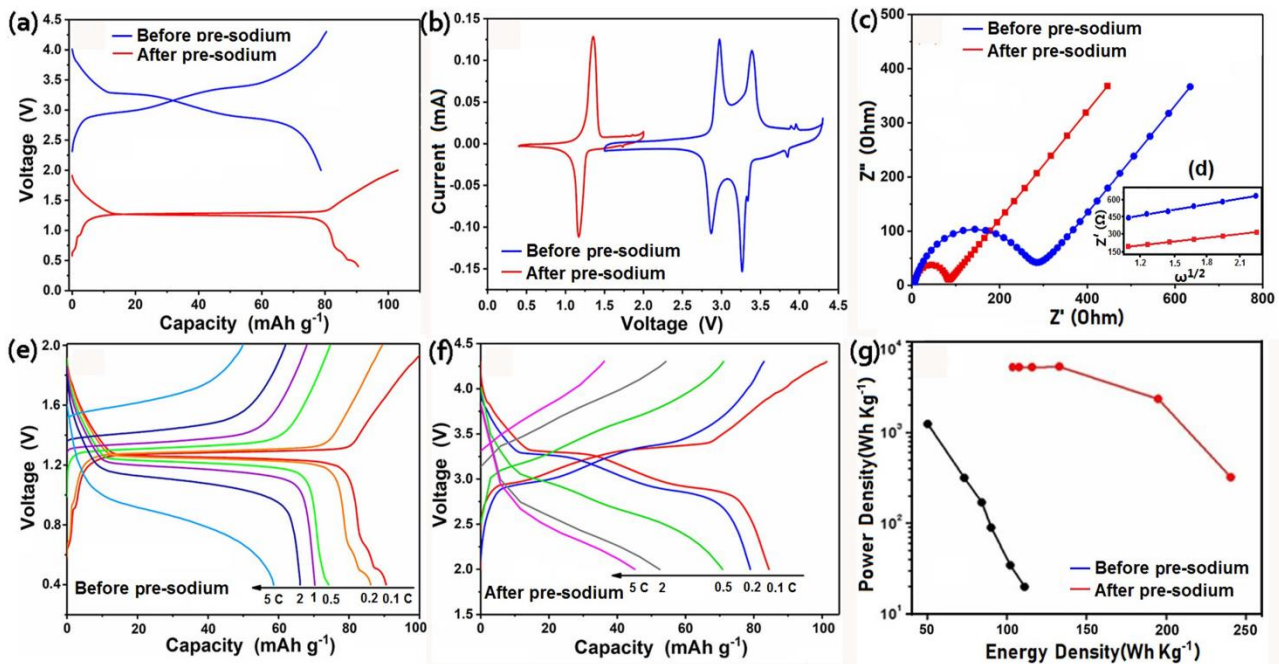
**Figure 7.** (a) The charge and discharge curve comparison of NTP/N-MHC//PNVP full battery before and after pre-sodium at 0.1 C. (b) The CV curve comparison of NTP/N-MHC//PNVP full battery before and after pre-sodium at the scan rate of 0.1 mV s-1. (c) The Nyquist plot comparison of NTP/N-MHC//PNVP full battery before and after pre-sodium,(d) shows the plots of impedance as a function of the inverse square root of angular frequency in the Warburg region. (ef) The charge and discharge curves of NTP/N-MHC//PNVP full battery before and after pre-sodium at different scan rates. (g) Ragone plot comparison of energy and power density of NTP/N-MHC//PNVP full battery before and after pre-sodium based on (e) and (f), showing the dependence of the energy density on the power density of the full cell.

after pre-sodium. The NTP/N-MHC//PNVP full battery after pre-sodium can achieve the ultrahigh energy density of 241 W h kg⁻¹ at a power density of 321 W kg⁻¹. When the ultrahigh power density increases to 5256 W kg⁻¹, its energy density still keeps 104 W h kg⁻¹ (Table S9), indicating that the pre-sodium is beneficial to the efficient ion/electron transport between the electrode and electrolyte. Furthermore, compared with the some recently reported SIFBs (Table S1), it can be concluded that the NTP/N-MHC//PNVP full battery after pre-sodium reaches the highest energy density with a markedly improved power density.

To expatiate the energy storage mechanism of NTP/N-MHC//PNVP full battery, we calculate adjustable parameter b value from the logarithmic plot of the peak current versus sweep rate. The b value is used to provide kinetic information about the electrochemical reactions of NTP/N-MHC//PNVP full battery. The range of b values from 0.5 to 1.0 indicates a "transition" area between the surface control process of pseudocapacitive materials and the diffusion control process of battery-type materials, and the capacitive contribution increases with increasing b value.[24] Figure 8a and Figure 8d shows the CV curves of NTP/N-MHC//PNVP full battery before and after pre-sodium at different sweep speeds, respectively. The logarithmic plot of the peak current (i) versus sweep rate (v) is indicative of the rate-limited characteristics by Equation (6): [25]

$$i = av^b \tag{6}$$

The slope $b$ value is calculated from the linear regression equation of Figure 8b and Figure 8e. The results show that the b-values of the cathode and anode peaks for the NTP/N-MHC//PNVP full batteries before pre-sodium were 0.53 and 0.54, respectively (Figure 8b). The $b$ values about 0.5 represent the larger contribution from diffusion-controlled intercalation processes that occur in the bulk, such as battery-type processes (Figure 8c).[24] The $b$-values of the cathode and anode peaks for the NTP/N-MHC//PNVP full batteries after pre-sodium were 0.72 and 0.82, respectively (Figure 8e), indicating the higher capacitive contribution of the surface control process (Figure 8f). These results explain the different energy storage mechanism of NTP/N-MHC//PNVP full batteries before and after pre-sodium. A rough estimate of the mixing processes of surface and diffusion-control can be done by Equation (7): [24]

$$i(v) = k_1 v + k_2 v^{1/2} \tag{7}$$

Where $k_1v$ is the contribution from surface capacitances and $k_2v^{1/2}$ is the contribution from diffusion-controlled processes. If divided both sides by $i/v^{1/2}$, this equation becomes Equation (8):

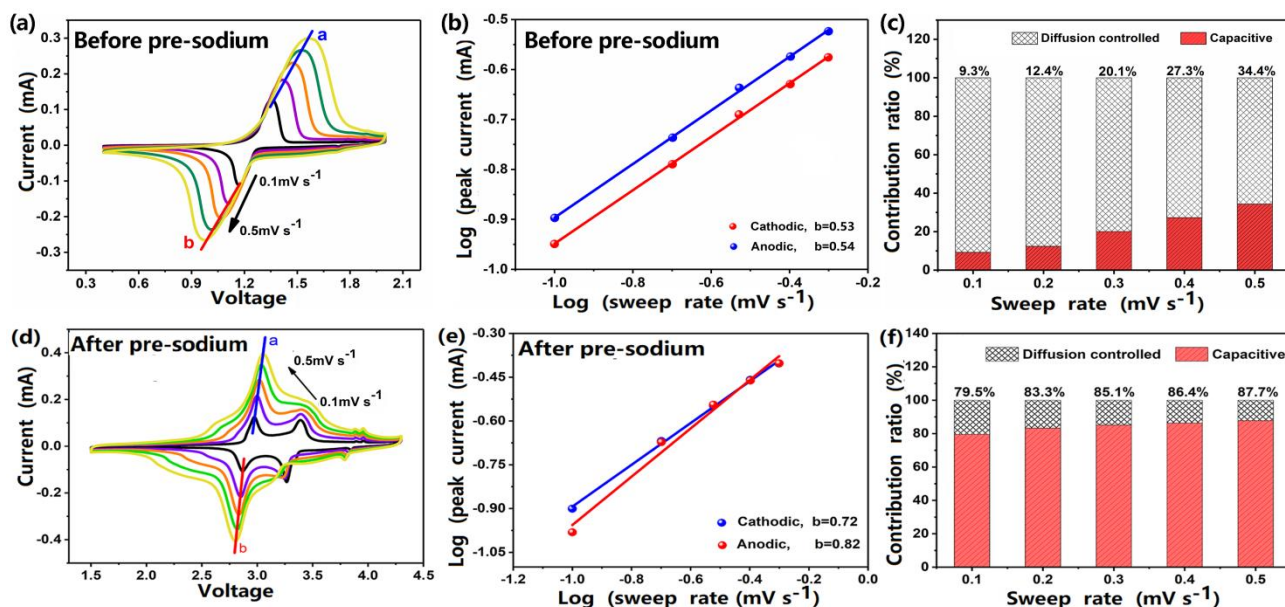$$i/v^{1/2} = k_1 v^{1/2} + k_2 \tag{8}$$

**Figure 8.** (a) The CV curves of NTP/N-MHC//PNVP full battery before pre-sodium in the voltage range of 0.3–2.1 V at various sweep rates. (b) Plots of log (sweep rate) versus log (peak current) before pre-sodium. (c) Capacitive contribution in the CV curves of NTP/N-MHC//PNVP full battery before pre-sodium obtained at different sweep rates. (d) The CV curves of NTP/N-MHC//PNVP full battery after pre-sodium in the voltage range of 1.5–4.5 V at various sweep rates. (e) Plots of log (sweep rate) versus log (peak current) after pre-sodium. (f) Capacitive contribution in the CV curves of NTP/N-MHC//PNVP full battery after pre-sodium obtained at different sweep rates after pre-sodium.

The specific data of $k_1$ and $k_2$ are calculated by the linear regression equation of $i/v^{1/2}$ to $v^{1/2}$. Therefore, the contribution rate of the two processes at a fixed potential is obtained. Using this approach, we can determine the proportion of the mixing processes in the entire potential window. As shown in Figure 8f, the surface control process accounted for 87.7% of the total Na ion storage at 0.5 mV s$^{-1}$. The capacitive contribution in the CV curves of NTP/N-MHC//PNVP full battery after pre-sodium obtained at different sweep rates is in the range of 79.5–87.7%, indicating that the NTP/N- MHC//PNVP full battery after pre-sodium has a higher capacitive contribution.

In order to investigate the effect of electrode mass loading on electrochemical properties, the charge and discharge curve comparison of NTP/N-MHC//PNVP full battery with different mass loading at 0.1 C is shown in Fig. S11a. Fig. S11b shows the cycle performance of NTP/N-MHC//PNVP full battery with anode mass loading of 1.5 mg cm$^{-2}$ and cathode loading of 1.8 mg cm$^{-2}$ at current density of 10 C. The result shows that the full cell with higher mass loading has poor cycle performance and lower Coulomb efficiency at 10 C than these of the NTP/N-MHC//PNVP full cell with anode mass loading of 1.2 mg cm$^{-2}$ and cathode loading of 1.3 mg cm$^{-2}$ at 20 C (Fig. 6d). The reasons are as follows: First, the increase of the mass loading leads to an increase of the actual current at the same current density, which also increases the charge-discharge polarization and reduce the capacity of the battery because of incomplete electrolyte penetration.[26] Fig.S11a shows that the full cell with anode mass loading of 1.5 mg cm$^{-2}$ and

cathode loading of 1.8 mg cm$^{-2}$ has the higher charge-discharge polarization than the full cell with anode mass loading of 1.2 mg cm$^{-2}$ and cathode loading of 1.3 mg cm$^{-2}$. Second, the slurry coating with high mass loading is easy to peel off, causing the battery to be unstable. Finally, the high mass loading also causes dendrites due to excess ions.

Based on the electrochemical performance analysis, an energy storage mechanism model of the NTP/N-MHC//PNVP full battery after pre-sodium is proposed, as shown in Figure S12. Its capacitive contribution (surface control process, 87.7%) in the sandwich structure dominated the total charge storage at a high sweep rate of 0.5 mV s$^{-1}$. This is due to the emergence of extrinsic faradaic reactions on the interface between NTP and N-MHC. These interfaces also provided a large accessible surface area for fast charge transfer and a shorter diffusion path for Na+ insertion/extraction at active species, thus significantly improving the power density. More importantly, NTP nanoparticles between two N-MHC ultrathin sheets can provide high Na ion storage interface and efficient electron/ion transport pathway for fast ion intercalation, which also played an important role in enhancing the energy density. Due to the collective and

synergetic effect of different energy storage control processes in the NTP/N-MHC with the unique sandwich structure, the NTP/N-MHC//PNVP full battery after pre-sodium utilized the hybrid energy storage mechanisms exhibit an ultrahigh energy density and an excellent power density.

# Conclusion

Here, sodium-ion full batteries (SIFBs) with ultrahigh energy/power densities are developed by using $NaTi_2(PO_4)_3$ (NTP)/N-doped mesoporous hard carbon (N-MHC) hybrid anode and porous $Na_3V_2(PO_4)_3$ (PNVP) cathode for the first time. The results show that chitosan biotemplate during synthesis can effectively induce nucleation of NTP nanoparticles, promote its two-dimensional cross-linking reaction and form N-MHC with sandwich structure. The NTP/N-MHC hybrid electrode endows the NTP/N-MHC//PNVP full battery with a hybrid energy storage mechanism because of its unique sandwich structural features. As a result, the NTP/N-MHC hybrid electrode for Na ion half batteries exhibits a ultrahigh reversible capacity (240 mAh $g^{-1}$ at 1 C, 109.7 mAh $g^{-1}$ at 100 C), ultrahigh energy/power densities (76.56 W h $kg^{-1}$/5104 W $kg^{-1}$) and a long cycle-life (capacity retention of 92.1% after 1000 cycles at 100 C) in a half cell and the relatively wide voltage range of 0.01–3.0 V. The NTP/N-MHC//PNVP full battery also showed high discharge capacity (95mAh $g^{-1}$) and long-term cycle life at 0.1 C (capacity retention at 20 C was 81% after 1000 cycles). Furthermore, the NTP/N-MHC//PNVP full battery after pre-sodium exhibits high energy/power densities (104 W h $kg^{-1}$/5256 W $kg^{-1}$). We hope this work can demonstrate that energy/power densities can be largely improved via the design of hybrid electrodes with unique structure, which provides new insights for realizing high performance SIFBs .

# Experimental

## Materials synthesis

Chitosan with deacetylation degree of 96% and acetic acid of 99.5% were purchased from Weihai Ziguang Technology Park Co., Ltd and Tianjin Fuyu Fine Chemical Co., Ltd. respectively. $NH_4H_2(PO_4)_3$ (99.9%), $Na_2CO_3$ (99.9%) and titanium butoxide (99.9%) were obtained from McLean Reagent Co., Ltd. Citric acid (99.5%) is from Tianjin Damao Chemical Co., Ltd.

The fabrication process of the NTP/N-MHC hybrid electrode by using chitosan biotemplate assisted sol-gel method is illustrated in Figure S1. Firstly, chitosan with different contents (100, 150, 200 and 250 mg) was first dissolved into 20 mL 1wt% acetic acid solution, respectively, forming different A solutions after magnetic stirring for 3 hours. $NH_4H_2(PO_4)_3$ (3.45 g), $Na_2CO_3$ (0.53 g) and titanium butoxide (6.81 g) were successively added to 40 ml 0.1 M citric acid solution, forming B solution after magnetic stirring for 4 hours. Then, the different A solutions were added into the B solution with vigorous stirring respectively. The forming mixture was further stirred to form a

jelly，and dried in the vacuum oven at 80 °C for 12 h. The products were finally annealed in the tube furnace under N2 atmosphere at 800 °C for 8 h to form the NTP/N-MHC-1 (100 mg Chitosan), NTP/N-MHC-2 (150 mg Chitosan), NTP/N-MHC-3 (200 mg Chitosan) and NTP/N-MHC-4 (250 mg Chitosan). For comparison, the NTP/C without the chitosan and the NTP without any carbon source were also synthesized by using the same method described above. The PNVP was prepared by using the previously reported method.[8]

## Characterization

The phase composition and crystal structure features of the different samples were analyzed by X-ray diffraction (XRD, Shimadzu-6100 with Cu Kα radiation over a range of 2θ angles from 10° to 70° at a scanning rate of 4° $min^{-1}$). The X-ray photoelectron spectroscopy (XPS) analysis was performed on a Thermo Fisher Scientific ESCALAB Xi spectrometer with Al Kα (1486.6 eV) as the X-ray source. The morphology and fine microstructure were observed on scanning/transmission electron microscopes (SEM, ZEISS Gemini 500, TEM, JEM- 2100 and STEM, X-MaxN TSR). The Raman spectra of NTP/C and NTP/N-MHC were recorded on the condition of 532 nm diode laser excitation (LabRam HR Evolution). The $N_2$ adsorption-desorption isotherms and Barrett-Joyner-Halenda pore size distributions were obtained at 77K using an automatic surface area analyzer (Micromeritics, Gemini V2380, USA) under continuous adsorption conditions.

## Electrochemical evaluation

The working electrode was prepared by spreading the slurry of the active materials (80 wt.%), acetylene black (10 wt.%) and PVDF binder (10 wt.%) on a Cu foil and dried at 110 °C in vacuum for overnight. The average mass loading of the NTP/N-MHC anode was about 1.5 mg $cm^{-2}$. CR 2032 coin cells were assembled in an argon-filled glove box. For the test of NTP/N-MHC half battery, sodium metal was used as the reference electrode, a solution of 1 M NaClO4 in EC: PC (1:1) + 5wt.% FEC as the electrolyte, and a Whatman glass microfiber filter (Grade GF/F) as the separator. The charge-discharge properties were tested on a Channels battery analyzer (CT3008W). The cyclic voltammetry (CV) and electrochemical impedance spectroscopy (EIS) were tested on a PARSTAT 2263 electrochemical workstation. The voltage range of CV measurements was 0.0–4.5 V.

Furthermore, the full battery (NTP/N-MHC//PNVP) was constructed using PNVP as the cathode and NTP/N-MHC-3 as the anode. The working electrode was prepared by spreading

the slurry of the PNVP (80 wt.%), acetylene black (10 wt.%) and PVDF binder (10 wt.%) on an Al foil and dried at 110°C in vacuum for overnight. The average mass loading of the PNVP cathode was about 1.2 mg cm$^{-2}$. The mass ratio between cathode and anode is about 1.2:1 so that the battery capacity was determined by the anode. The charge and discharge measurements were carried out between 0.0–4.5 V. All the tests were performed at room temperature.

## Acknowledgements

## Conflicts of interest

There are no conflicts of interest to declare.
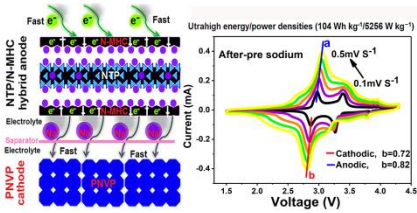
**Keywords:** supercapacitor hybrid device · NaTi$_2$(PO$_4$)$_3$ · N-doped mesoporous hard carbon · sandwich structure · chitosan

## References

1  a) H. Su, H. Huang, S. Zhao,Y. Zhou, S. Xu, H. Pan, B. Gu, X. Chu, W. Deng, H. Zhang, H. Zhang, J. Chen, W. Yang, ACS Appl. Mater., 2019, 10.1021/acsami.9b15781; b) W. Liu, J. Li, K. Feng, A. Sy, Y. Liu, Y. Lim, G. Lui, R. Tjandra, L. Rasenthiram, G.  Chiu, A. Yu, 2016, 9, 25941−25953.

2  a) F. Zhang, H. Gao, J. Hao, A. Zhang, P. Li, Y. Liu, j. Chen, Z. Guo, Adv. Funct Mater., 2019, 29, 1808291; b) S. Wu, C. Liu, D.A. Dinh, S. Hui, K, N, Hui, J,M, Yun, K,H, Kim, ACS Sustainable Chem. Eng., 2019, 7, 9763−9770; c) S. Wu, H. Guo, K.S. Hui, K.N. Hui, Electrochimica Acta, 2019, 2, 759−768; d) S. Liu, Di. Ni, H.F. Li, K.N. Hui, C.-Y. Ouyang, S.C. Jun, J. Mater. Chem.A., 2018, 8, 10674−10685.

3  a) H.C. Tang, Y.L. Yuan, L. Meng, W.C. Wang, J.G. Lu, Y.J. Zeng, T.Q. Huang, C. Gao, Adv. Mater. Technol-us., 2018, 7, 1800074; b) J. Fan, K.R. Lin, J. Wang, R.F. Ma, B.G. Lu, Adv. Mater., 2018, 30, 1800804; c) Z.B. Zhai, K.J. Huang, X. Wu, Nano Energy, 2018, 47, 89−95; d) Y. Ouyang, H.T Ye, X.F. Xia, X.Y. Jiao, G.M. Li, S. Mutahir, L. Wang, D. Mandler, W. Lei, Q.l. Hao, J. Mater. Chem. A., 2019, 7, 3228−3237; e) L. Ye, Y.T. Zhou, Z.P. Bao, Y.G. Zhao, Y.N. Zou, Y. Zhao, Q. Jiang, J. Mater. Chem. A., 2018, 39, 19020−19029; f) L.B. Zhang, Y.Y. Zhang, S.L. Huang, Y.L. Yuan, H. Li, Z.G. Jin, J.H. Wu, Q.F. Liao, Li. Hu, J.G. Lu, S.C. Ruan, Y.J. Zeng, Electrochim Acta, 2018, 281, 189−197.

4  S.Liu, Y.Yin, M.Wu, K.S. Hui, K.N. Hui, C.Y. Ouyang, S.C. Jun, Small, 2019,15,1803984.

5  L.Zhang, K.N. Hui, K.S. Hui, S.W. Or, Dalton Trans., 2019, 48, 150−157;

6  a) Y.Y. Wang, B.H. Hou, J.Z. Guo, Q.L. Ning, W.L. Pang, J.W. Wang, C.L. Lü, X.L. Wu, Adv. Energy Mater., 2018, 8, 1703252; b) C.L. Jiang, Y. Fang, W.Y. Zhang, X.H. Song, J.H. Lang, L. Shi,  Y. Tang, Angew. Chem., Int. Ed., 2018, 57, 16370−16374; c) B.H. Hou, Y.Y. Wang, J.Z. Guo, Q.L. Ning, X.T. Xi, W.L. Pang, A.M. Cao, X. Wang, J.P. Zhang, X.L. Wu, Nanoscale, 2018, 10, 9218−9225;

7  a) C.C. Wang, D.F. Du, M.M. Song, Y.H. Wang, F.J. Li, Adv. Energy Mater., 2019, 9, 1900022; b) Y.N. Zhou, P.F. Wang, X.D. Zhang, L.B. Huang, W.P. Wang, Y.X. Yin, S. Xu, Y.G. Guo, ACS Appl. Mater., 2019, 11, 24184−24191;

8  a) K.L. Zhang, X.D. Zhang, W. He, W.N. Xu, G.G. Xu, X.L. Yi, X.N. Yang, J.F. Zhu, J. Mater. Chem. A., 2019, 7, 9890−9902; b) Z. Jian, W. Han, X. Lu, H. Yang, Y.S. Hu, J. Zhou, Z. Zhou, J. Li, W. Chen, D. Chen, Adv. Energy Mater., 2013, 3, 156−160; c) Y. Fang, L. Xiao, X. Y. Cao, H. Yang, Adv. Mater., 2015, 27, 5895−5900.

9  Q. Yang, S. Cui, Y. Ge, Z. Tang, Z. Liu, H. Li, N. Li, H. Zhang, J. Liang, C. Zhi, Nano Energy, 2018, 50, 623−631;

10  a) C. Wu, P. Kopold, Y.L. Ding, P.A. van Aken, J. Maier, Y. Yu, ACS Nano, 2015, 9, 6610−6618; b) Q. Hu, M. Yu, J.Y. Liao, Z.Y. Wen, C.H. Chen, J. Mater. Chem. A., 2018, 5, 2365−2370; c) L. Wang, B. Wang, G.J. Liu,T.F. Liu, T.T. Gao, D.L. Wang, RSC Adv., 2016, 6, 70277−70283;

11  a) G.Z. Yang, H.W. Song, M.M Wu, C.X. Wang, J. Mater. Chem. A., 2015, 36, 18718−18726; b) G. Pang, P. Nie, C.Z. Yuan, L.F. Shen, X.G. Zhang, H.S. Li, C.L. Zhang, J. Mater. Chem. A., 2014, 48, 20659−20666; c) D.X. Wang, Q. Liu, C.J. Chen,  M.L. Li, X. Meng, X.F. Bie, Y.J. Wei, Y.H. Huang, F. Du, C.Z. Wang, G. Chen, ACS Appl. Mater., 2016, 8, 2238−2246.

12  C. Xu, Y. Xu, C.J. Tang, Q.L. Wei, J.S. Meng, L. Huang, L. Zhou, G.B. Zhang, L. He, L.Q. Mai, Nano Energy, 2016, 28, 224−231.

13  H.K. Roh, H.K. Kim, M.S. Kim, D.H. Kim, K.Y.  Chung, K.C. Roh, K.B. Kim,  Nano Research, 2016, 9, 1844−1855

14  a) Y. Chen, N.Q. Liu, H.Y. Shao, W.K. Wang, M.Y. Gao, C.M. Li, H. Zhang, A.B. Wang, Y.Q. Huang, J. Mater. Chem. A., 2015, 29, 15235-15240; b) L. Ma, X.p. Zhou, L.M. Xu, X.Y. Xu, L.L. Zhang, W.X. Chen, Electrochim Acta, 2015, 167, 39−47; c) D. Xu, J. Jin, C.H. Chen, Z.Y. Wen, ACS Appl. Mater., 2018, 10, 38526−38537; d) J. Duan, S.Y. Deng, W.Y. Wu, X. Li, H.Y. Fu, Y.H. Huang, W. Luo, ACS Appl. Mater., 2019, 11, 12415−12420; b) R.W. Mo, D. Rooney, K.N. Sun, H.Y. Yang, Nat. Commun., 2017, 7, 13949;

15  a) L. Wang, C.L. Yang, S. Dou, S.Y. Wang, J.T. Zhang, X. Gao, J.M. Ma, Y. Yu, Electrochim Acta, 2016, 219, 592–603; b) Z.Z. Yan, W. He, X.D. Zhang, X.N. Yang, Y Wang, X Zhang, Y Lou, G Xu, J. Mater. Sci.- Mater. Electron., 2019, 30, 4527−4540; c) X.Y. Jiang, Z.Q. Zeng, L.F. Xiao, X.P. Ai, H.X. Yang, Y.L. Cao, ACS Appl. Mater., 2017, 9, 43733−43738.

16  Y. Xu, Q.L. Wei, C. Xu, Q.D. Li, Q.Y. An, P.F. Zhang, J.Z. Shang, L. Zhou, L.Q. Mai, Adv. Energy Mater., 2016, 16, 1600389.

17  Z.Y. Wang, W. He, X.D. Zhang, Y.Z. Yue, G.H. Yang, X.L. Yi, Y.Y. Wang , J.C. Wang, ChemElectroChem, 2017, 4, 1600818.

18  X.D. Zhang, Z.Y. Bi, W. He, G. Yang, H. Liu, Y.Z. Yue, Energy Environ. Sci., 2014, 7, 2285−2294.

19  X.Y. Du, W. He, X.D. Zhang, Y.Z. Yue, H. Liu, X.G. Zhang, D.D. Min, X.X. Ge, Y. Du, J. Mater. Chem., 2012, 22, 5960−5969.

20  Z. Liu, Y. An, G. Pang, S. Dong, C. Xu, C. Mi, X. Zhang, Chem. Eng. J., 2018, 353, 814−823.

21  Y.J. Fang, L.F. Xiao, J.F. Qian, Y.L. Cao, X.P. Ai, YH. Huang, H.X. Yang, Adv. Energy Mater., 2016, 6, 1502197.

22  Z.Y. Wang, W. He, X.D. Zhang, Y.Z. Yue, J.H. Liu, C.J. Zhang, L.Y. Fang, J. Power Sources, 2017, 366, 9−17

23  Y.J. Zhang, F. Du, X. Yan, Y.M. Jin, K. Zhu, X. Wang, H.M. Li, G. Chen, C.Z. Wang, Y.J. Wei, ACS Appl. Mater., 2014, 6, 4458−4465.

24  J.L. Liu, J. Wang, C.H. Xu, H. Jiang, C.Z. Li, L.L. Zhang, J.Y. Lin, Z.X. Shen, Adv. Sci., 2018, 5, 1700322.

25  V. Augustyn, J. Come, M.A. Lowe, J.W. Kim, P.L. Taberna, S.H. Nat Mater., 2013, 12, 518−22.

26  G.A. Elia, I. Hasa, J. Hassoun, Electrochimica Acta, 2016, 191, 516−520.

2 **Entry for the Table of Contents**



3
4
5 **Na-ion battery-supercapacitor hybrid devices:** A high-performance hybrid device is developed by using $NaTi_2(PO_4)_3$/N-doped

6 mesoporous hard carbon (NTP/N-MHC) hybrid anode with unique sandwich and mesoporous structural features and porous

7 $Na_3V_2(PO_4)_3$ (PNVP) cathode. The hybrid device after pre-sodium shows high capacitive contribution, fast rate performance, utrahigh

8 energy/power densities and a long cycle-life.